An Eastward Current Encircling Mercury

Q. Shi[1, 2]†, Z. J. Rong[1, 2, 3]*†, S. Fatemi[4], J. A. Slavin[5], L. Klinger[6], C. Dong[7,8], L. Wang[7,8], J. Zhong[1,2,3], J. M. Raines[5], M. Holmström[9], C. J. Yuan[1,2,3], S. Barabash[9] and Y. Wei[1,2,3]

[1]Key Laboratory of Earth and Planetary Physics, Institute of Geology and Geophysics, Chinese Academy of Sciences; Beijing 100029, China.

[2]College of Earth and Planetary Sciences, University of Chinese Academy of Sciences; Beijing, China.

[3]Mohe Observatory of Geophysics, Institute of Geology and Geophysics, Chinese Academy of Sciences; Beijing, China.

[4]Department of Physics at Umeå University; Umeå, Sweden.

[5]Department of Climate and Space Sciences and Engineering, University of Michigan; Ann Arbor, MI, USA.

[6]Beijing International Center for Mathematical Research, Peking University; Beijing, China.

[7]Princeton Plasma Physics Laboratory, Princeton University; Princeton, NJ, USA.

[8]Department of Astrophysical Sciences, Princeton University; Princeton, NJ, USA.

[9]Swedish Institute of Space Physics; Kiruna, Sweden.

*Corresponding author: Z. J. Rong (rongzhaojin@mail.iggcas.ac.cn)

†These authors contributed equally to this work.

Key Points:

- We discovered an eastward current encircling Mercury on the night side for the first time.
- The eastward current can be well reproduced by hybrid simulations and well fits the signatures found in previous studies.
- The eastward current could be a diamagnetic current driven by a plasma pressure peak, and becomes more significant when IMF is northward.

This is the author manuscript accepted for publication and has undergone full peer review but has not been through the copyediting, typesetting, pagination and proofreading process, which may lead to differences between this version and the Version of Record. Please cite this article as doi: 10.1029/2022GL098415.

Abstract

Mercury has a terrestrial-like magnetosphere which is usually taken as a scaled-down-version of Earth's magnetosphere with a similar current system. We examine Mercury's magnetospheric current system based on a survey of Mercury's magnetic field measured by the Mercury Surface, Space Environment, Geochemistry, and Ranging (MESSENGER) spacecraft as well as computer simulations. We show that there is no significant Earth-like ring current flowing westward around Mercury, instead, we find, for the first time, an eastward current encircling the planet near the night-side magnetic equator with an altitude of ~500–1000 km. The eastward current is closed with the dayside magnetopause current and could be driven by the gradient of plasma pressure as a diamagnetic current. Thus, Mercury's magnetosphere is not a scaled-down Earth magnetosphere, but a unique natural space plasma laboratory. Our findings offer fresh insights to analyze data from the BepiColombo mission, which is expected to orbit Mercury in 2025.

Plain Language Summary

Whether Mercury possesses an Earth-like ring current has long been the focus of controversy in planetary science and space science. Here, based on the statistical analysis of the magnetic field measured by MESSENGER, we show that Mercury has no significant Earth-like ring current which flows westward around the planet, but we discover for the first time that there is an eastward current encircling the planet near the night side. Our discovery is verified by computer simulations and shows well consistence with the observation signatures found in previous studies. Our discovery updates the knowledge of the current system of Mercury's magnetosphere and demonstrates that the Mercury's magnetosphere cannot be simply seen as a scaled-down-version of Earth's magnetosphere.

1 Introduction

Early exploration of Mercury, based on data collected by Mariner 10 during its three flybys, revealed that it was the only terrestrial planet in our solar system, other than Earth, to possess a global dipolar magnetic field (Ness et al., 1974). A subsequent mission known as MErcury Surface, Space Environment, GEochemistry, and Ranging (MESSENGER), sent the first spacecraft to orbit around Mercury (Solomon et al., 2007). It confirmed the dipolar field and found it was similar to Earth's in that the magnetic field lines of Mercury are divergent near the south pole and convergent toward the north pole; Mercury's dipole moment, however, is only about 195±10 nT R_M^3 (R_M = 2440 km is the radius of Mercury)—much weaker than Earth's (4/10000 of Earth's dipole moment)—and Mercury's dipole center is shifted northward by about 484±11 km (0.2 R_M) (Anderson & Johnson et al., 2011). Further, Mercury has no atmosphere but possesses a tenuous surface-bounded exosphere. As the closest planet to the Sun, Mercury encounters a much stronger impingement of solar wind, whose density and dynamic pressure are an order of magnitude higher than those at Earth. In comparison to Earth, the result is a much smaller, weaker and more dynamic magnetosphere (Dong et al., 2019; Slavin et al., 2008; Winslow et al., 2013).

It is well-known that Earth's magnetic field can be well-approximated by a dipole field within a radial distance of about six Earth radii. Energetic charged particles (ions ranging in energy from 1 keV to 200 keV, and electrons of <10 keV) can be trapped by this dipole field, and drift azimuthally around Earth due to the magnetic field's gradient and curvature (Northrop, 1963). This drift results in a westward ring current providing a reservoir of energetic particles

that can damage or "kill" Earth satellites and induce field disturbances in the planet's space environment (Daglis, 2006).

It has been debated whether Mercury could have a similar ensemble of trapped charged particles that, analogous to the Earth's ring current, drift as a westward current around the planet because the weaker dipolar field of Mercury cannot trap ions in the energy range typical of Earth's ring current owing to the larger gyro–radius (Walsh et al., 2013). However, simulations and observations have demonstrated that plasma at the energy range of 1–10 keV could be quasi-trapped in Mercury's inner magnetosphere of Mercury (Walsh et al., 2013; Yagi et al., 2010; Müller et al., 2012; Schriver et al., 2011 and Ho et al., 2016; Herčík et al.,2015). Nonetheless, we still lack sufficient data to know whether these quasi-trapped particles can drift around Mercury to form a significant ring current, and otherwise what associated current system would be driven in Mercury's magnetosphere.

Here, based on a statistical analysis of MESSENGER data, we report that there is no significant westward ring current around Mercury, instead, we find an eastward current (EC) on the near-Mercury night side.

2 Materials and Methods

2.1 Coordinate system.

In the Mercury Solar Orbital (MSO) coordinate system, the origin is at the planet center, +x points sunward, +z points to the north pole, and +y completes the right-hand coordinate system. In our study, both datasets of magnetic field and locations of spacecraft in MSO have to be transformed into a modified coordinate system which is referred to as aberrated Mercury Solar Magnetospheric (aMSM) coordinates. In aMSM, the origin is at the dipole center, which is shifted northward from the planet center by 0.198 R_M (484 km). The direction of the +x-axis is antiparallel to the flow direction of the upstream solar wind, the +z-axis points to the North Pole, and the +y-axis completes the right-hand coordinate system. The plane of z = 0 in aMSM is referred to as the magnetic equatorial plane. The aberration effect brought by Mercury's orbital motion has been considered in aMSM, where the upstream solar wind flow velocity is assumed to be a typical radial speed, 400 km/s, plus the transverse velocity of Mercury's orbital motion, v, which is roughly estimated by $\frac{m_P v^2}{R_{MS}} = \frac{GM_S m_P}{R_{MS}^2}$, where R_{MS} is the distance of Mercury to the Sun, m_P is the mass of Mercury, M_S is the mass of the Sun, and G is the gravitational constant. In the frame of aMSM, it is convenient to define a spherical coordinate system, where the azimuthal coordinate or longitude ϕ ($0 \le \phi \le 360°$) increases azimuthally from the +x-axis toward the +y-axis, while the polar angle θ ($0 \le \theta \le 180°$) increases from the +z-axis toward the -z-axis. The latitude equals $90° - \theta$. In our study, the aMSM coordinates and the associated spherical coordinates are used unless otherwise stated.

2.2 Data usage.

The magnetic field vector data (where time resolution is 1 second) used in this study is taken from measurements made by the magnetometer (MAG, Anderson et al., 2007) onboard the MESSENGER spacecraft. The plasma dataset, with a time resolution of 1 minute, consists of proton number density, temperature, and thermal pressure (NTP, Gershman et al., 2013; Sun et al., 2016; Zurbuchen et al., 2013), derived from measurements recorded by the Fast Imaging

Plasma Spectrometer (FIPS, Andrews et al., 2007) onboard MESSENGER (see Figure S1). The FIPS NTP data set is recovered from a series of isotropic, stationary Maxwellian distributions corresponding to the *E/q* spectra that matched the orbital observations (Gershman et al., 2013; Sun et al., 2016 and Zurbuchen et al., 2013). Data points of the FIPS NTP dataset were used when their quality was GOOD (that is, their quality flag was zero). In our study, all distribution maps of datasets displayed were derived by averaging with bins of 0.1×0.1×0.1 R_M^3.

2.3 Calculation of current density.

Owing to limitations of the FIPS field of view, plasma moments, such as density (N_i) and velocity ($\boldsymbol{V}_i$), are hard to derive unless reasonable assumptions of ion spectra are made (Raines et al., 2011). Thus, it is challenging to calculate the accurate current density directly from ion moments. Given the magnetic field derived from data amassed by MESSENGER during the orbiting period (23 March 2011–30 April 2015, see Figure S2), we can make important headway in characterizing the current density morphology simply by taking the curl of the statistically determined magnetic field, viz., $\boldsymbol{J} = (\nabla \times \boldsymbol{B})/\mu_0$. This method of calculating average current density by taking the curl of the magnetic field has been used to study the morphology of Earth's ring current (Le et al., 2004) and the cross-tail current in Mercury's magnetotail (Rong et al., 2018). In our calculation, the spatial domain of the inner magnetosphere, centered at the origin of aMSM, is set as $X \times Y \times Z$ = 6 R_M × 6 R_M × 6 R_M. The spatial domain is partitioned by bins of 0.1 R_M ×0.1 R_M ×0.1 R_M. In each bin, the magnetic field is calculated by averaging all data points in the bin, and the position of the average bin field is set at the center of the bin. Based on $\boldsymbol{J} = (\nabla \times \boldsymbol{B})/\mu_0$, the three current density components are calculated by $(J_x, J_y, J_z) = (\frac{\partial B_z}{\partial y} - \frac{\partial B_y}{\partial z}, \frac{\partial B_x}{\partial z} - \frac{\partial B_z}{\partial x}, \frac{\partial B_y}{\partial x} - \frac{\partial B_x}{\partial y})/\mu_0$. Differences are approximately derived through central difference; forward difference and backward difference are used at boundaries. The azimuth component of the current density J_ϕ is correspondingly calculated as $J_\phi = -J_x \sin\phi + J_y \cos\phi$, where ϕ is the azimuth angle. Since the dipole field makes no contribution here, one may subtract it to calculate the current density. We found, indeed, that when the dipole field is subtracted the resulting current density map shows little change (not shown here). Note, due to the insufficient orbital coverage nearby Mercury, we did not categorize the dataset according to a given criterion, e.g. the polarity of the interplanetary magnetic field (IMF) B_z component.

2.4 Simulation.

To simulate the interaction between the solar wind and Mercury, we use the Amitis simulation code, the first three-dimensional (in both configuration and phase space), time-dependent hybrid plasma model that runs entirely on Graphics Processing Units (GPUs, Fatemi et al., 2017, 2020; Fatemi, Poirier, et al., 2018; Fatemi & Poppe, 2018 and Fuqua et al., 2019). In this model, the ions are charged macro-particles and the electrons are a mass-less charge neutralizing fluid. The Lorentz force and the equation of motion are used to calculate particle trajectories in time. The electric field, $\boldsymbol{E}$, is calculated directly from the electron momentum equation. Faraday's law, $\frac{\partial \boldsymbol{B}}{\partial t} = -\nabla \times \boldsymbol{E}$, is used to advance the magnetic field $\boldsymbol{B}$ in time. The model has been applied successfully to studies of interactions between the solar wind plasma and the Moon (Fatemi et al., 2017; Fuqua et al., 2019 and Rasca et al., 2021), Mercury (Fatemi, 2020 and Aizawa et al., 2021), and the asteroid 16 Psyche (Fatemi & Poppe, 2018). In our simulations, Mercury is assumed to be a spherical object of radius R_M = 2440 km with no exosphere and a

surface that is a perfect plasma absorber. The planet center coincides with the origin of the coordinates, and a magnetic dipole (oriented along the -z-axis) with the dipole moment of 195 $nT \cdot R_M^3$ is displaced 484 km northward from the planet center. The solar wind, whose composition is assumed to be protons only, flows toward the -x axis.

3 Results

3.1 The distribution of current density.

The calculated current density in the equatorial plane of Mercury shows a pattern similar to that of Earth's magnetospheric current system (Figure 1a). One can identify the magnetopause current or Chapman–Ferraro current, $\boldsymbol{J}_{CF}$, flowing eastward at the dayside magnetopause, and the cross-tail current, $\boldsymbol{J}_{CT}$, flowing duskward on the night side beyond the radial distance 1.4 R_M. The Chapman–Ferraro current and cross-tail current have also been reproduced and reported in previous simulations (Glassmeier, 2000) and data analysis (Rong et al., 2018). However, in contrast to the Earth's ring current derived by taking the curl of Earth's statistically determined magnetic field (Le et al., 2004), we do not find a significant westward ring current around Mercury. Unexpectedly, we noticed the presence of an eastern-directed current on Mercury's night side, with radial distance ~1.2–1.4 R_M.

3.2 Characteristics of Mercury's Eastward Current.

It is informative to analyze the global distribution map of the EC on which the streamlines of the average current density within the distance 1.2–1.4 R_M are displayed on the spherical surface (Figure 1b). It is worth noting that the EC on the night side (red streamlines with 18:00<LT<06:00) is distributed mainly around the magnetic equatorial plane and closes with the dayside Chapman–Ferraro current. The EC (10~40 nA m^{-2}) is weaker on average than the dayside Chapman–Ferraro current (>60 nA m^{-2}).

3.3 Simulation results.

To analyze the validity of the EC we have detected, we use Amitis, a three-dimensional global hybrid model (consisting of kinetic ions and fluid electrons, Fatemi et al., 2017) to study the interaction of Mercury with the solar wind (see subsection 2.4). The current density, $\boldsymbol{J}$, that the simulation yields is calculated by $\boldsymbol{J} = \nabla \times \boldsymbol{B}/\mu_0$. We performed our simulations under three typical solar-wind conditions: when theIMF points northward, southward, and when the dynamic pressure of the solar wind becomes higher, respectively (Figure 2 and Table 1).

Consistent with data analysis (Figure 1), the morphology and strength of the observed EC can be reproduced by our simulations, no matter whether the IMF points northward or southward; as is shown in Figure 2, the simulated EC does indeed concentrate around the magnetic equatorial plane. We find that the simulated EC near midnight is closer to the surface of Mercury but moves to higher altitudes near the terminator to close with the magnetopause current (Figure 2a, 2d and 2g), this appears consistent with the typical trajectory of hot ions in the Alfvén layer of inner magnetosphere combining the sunward magnetospheric convection and westward magnetic drift (Alfvén & Fälthammar, 1963). Comparing both simulation cases, the EC appears more significant when the IMF is northward. The associated spatial distribution of plasma is crescent-shaped, and the ion density seems denser in the northward IMF (Figure 2c, 2f and 2i). The simulations also show that the EC would be stronger when the solar wind has higher

dynamic pressure(Figure 2g and 2h), however, an EC is always detectable regardless of the IMF orientation (Figure 2, Figure S3 and Table S1).

4 Discussion

4.1 Mechanism of the eastward current.

An eastward ring current in Earth's magnetosphere has been reported by numerous observational studies and simulations (Shen et al., 2014; Yang et al., 2016), which could be driven by a plasma pressure peak circumscribed by the inner magnetosphere (Liemohn et al., 2013). Such plasma peak was formed by hot ions trapped on closed drift paths around Earth because of magnetic gradient-curvature drifting (Liemohn et al., 2013). Similarly, it might be reasonable to ascribe the formation of EC nearby Mercury to a plasma pressure peak encircling the planet. Because the magnetic field, $\boldsymbol{B}$, in Mercury's magnetic equatorial plane is northward, and the plasma pressure gradient near the planet's surface, ∇P, is radially outward-pointing to the pressure peak (Korth et al., 2012, 2014), the locally generated diamagnetic current, $\boldsymbol{J} = (\boldsymbol{B} \times \nabla P)/B^2$, points eastward (Parker, 1957) (Figure 3). Several types of evidence support this picture.

First, the plasma pressure observed by MESSENGER (Raines et al., 2011, 2013) shows a sharp inner boundary near the dawn terminator (Figure 1c), which coincides with the location of the significant EC that we have found (Figure 1a). Meanwhile, the location of the inner boundary of simulated plasma density on the night side is nearly coincident with that of JEC(see Figure 2).

Second, numerous simulations have demonstrated that a plasma belt could appear on the nightside near Mercury (Walsh et al., 2013; Müller et al., 2012), and data analysis also has shown that a plasma population of energy 1-10 keV can be trapped on the night side with distance ~1.4 R_M (Schriver et al., 2011 and Ho et al., 2016).

Third, the magnetic fields recorded by MESSENGER during its first and second flybys consistently imply the presence of a plasma belt (Figure S4). In the first flyby, MESSENGER recorded two magnetic field depressions, at midnight and near the terminator respectively (Figure S4b). Such diamagnetic decreases are consistent with the presence of hot plasma, as first noted by Slavin et al (2008). Similar diamagnetic decreases were reported in the second flyby (Anderson & Slavin et al., 2011, Figure S4c). Note that the estimated currents of these diamagnetic decreases near the terminator were roughly 244 nA m^{-2} (186 nA m^{-2}) for the first (second) flyby, much larger than estimated by the curl of the average magnetic field (Figure 1). In other words, our curl-technique may underestimate the EC, because the average of the data in the bin would smooth the field spatial variation leading to the underestimate of $\nabla \times$B.

Using the MESSENGER NTP dataset (Figure S1), we have evaluated and compared the different ion drift motions contributing to the EC (Text S1 and S2). Our calculations demonstrate that the EC is due primarily to the diamagnetic current (Text S1, S2, and Figure S5) and further indicate that the main factor controlling the EC could be the plasma density gradient if the ions and electrons are at the same temperature (Text S2, and Figure S6).

Beyond the simulation results, several other points relevant to understanding the formation of an EC are worth noting.

4.2 Plasma sources.

In both our simulations and previous simulations (Müller et al., 2012), the only ion source considered has been the solar wind protons. However, in reality, one may not rule out the possible contribution of planetary ions to the EC. Slavin et al (2008). have suggested that the diamagnetic decrease of the magnetic field near the dawn side could be induced by hot planetary ions. Those ions are generated by photon-ionization and enter inside the dayside magnetopause after being picked up and accelerated by the fast solar wind in the magnetosheath. On the night side, the impact ionization of the exosphere by hot electrons from the plasma sheet may create planetary ions near the surface, which may contribute to the plasma pressure peak. Note that, the ions of Na^+ group in the magnetosphere, though of planetary origin, have been observed preferentially in the dusk-side of the magnetotail (Raines et al., 2013); thus, the ion of Na^+ group probably does not contribute significantly to the creation of the EC on the dawn-side.

4.3 Dependence on the polarity of IMF Bz.

The simulation by Herčík et al.(2015) suggested that the major source of the plasma peak is the solar wind ions coming from the current sheet, entering the inner magnetosphere by the magnetospheric flanks. Our simulation shows that solar wind can enter the plasma sheet through both flanks (Figure S7), and the presence of the EC is more significant when the upstream IMF is northward (Figure 2). Thus, it seems that a northward IMF favors the entry of solar wind into Mercury's magnetosphere, which is very similar to the case of Earth where solar wind easily enters Earth's magnetosphere via both flanks when the IMF is northward, resulting in the Cold-Dense Plasma Sheet (Fujimoto et al., 1997). Note that the estimated EC for flyby 1, at the time of a northward IMF, is larger than that for flyby 2, under a southward IMF condition (Figure S4). Several mechanisms have been presented to account for the entry of solar wind into Earth's magnetosphere under a northward IMF, such as diffusion of the solar wind across both flanks (Terasawa et al., 1997), the capture of the solar wind by Kelvin-Helmholtz instability (Hasegawa et al., 2004), and poleward-of-cusp reconnection (Song & Russell, 1992). Given the presence of an EC regardless of IMF orientation, and the preference of Kelvin-Helmholtz instability at the dusk flank of Mercury's magnetosphere (Sundberg et al., 2012; Paral & Rankin, 2013), we suggest that the diffusion of solar wind across both flanks is the main source of EC, a diffusion that becomes more significant when the IMF is northward. Additionally, since the more stretched magnetospheric field lines under a southward IMF do not favour the trapping of plasma, this could perhaps explain also the less significant EC during southward IMF. Some simulations suggested that the solar wind ions could enter through the diffusion in the cusps and move westward owing to magnetic drift and eventually hit the surface in the nightside [Mura et al.,2005; Kallio et al.,2008]. It is unknown whether the solar wind ions from cusp could contribute to the formation for EC. More works are needed to address this issue.

4.4 Dawn–dusk asymmetry.

Our statistics in Figure 1 show that the EC is stronger on the dawn side (~40 nA m^{-2} in local time 03:00–07:00) relative to that on the dusk side (~20 nA m^{-2} in local time 18:00–20:00). There are two possible explanations of this dawn-dusk asymmetry: First, it could be merely a misleading consequence of incomplete coverage by the spacecraft near the nightside surface. Because most orbits crossing the dawn (dusk) side of the EC occurred near aphelion (perihelion)

(Figure S8), the bias of heliocentric distance may result in apparent asymmetry. Second, the asymmetry is a real pattern of the EC. Similar dawn-dusk asymmetries in plasma pressure and density have been noticed in previous simulations (Müller et al., 2012) and calculations (Yagi et al., 2010), and in observations of quasi-trapped ions (Schriver et al., 2011) and suprathermal electrons (Ho et al., 2016). The future survey of BepiColombo with wider orbital coverage in the inner magnetosphere could clarify this issue.

4.5 The formation of plasma pressure peak

The reason to generate the formation of plasma pressure peak is an open issue. The injected solar wind protons from both tail flanks, would be moved under the sunward convection and the westward magnetic-drift motion. The gyroradius loss of protons due to crossing the dayside magnetopause or impacting with Mercury's surface on the night side could contribute to the formation of the pressure peak. For example, in our simulations, the empty low altitude "wake" on the dayside (see Figure 2a-2b) appears consistent with some of the sunward flow (or ExB drift paths) intersecting the surface of Mercury on the nightside. The loss of solar wind protons into the planetary surface on the night side may contribute to creating the outward plasma pressure gradient that drives EC.

4.6 The scenario of EC generation.

Based on the analysis above, we may present a scenario to elucidate the generation of the EC. Regardless of the IMF orientation, the interaction between Mercury and the solar wind allows entry of solar wind particles into Mercury's plasma sheet via plasma diffusion through both flanks; but entry by diffusion becomes more significant when the IMF is northward. Once solar wind ions enter Mercury's magnetosphere and are trapped by the magnetospheric field lines, the motion of ions would be regulated simultaneously by sunward magnetospheric convection and westward magnetic gradient-curvature drift motion. In this case, the entering solar wind ions would drift both sunward and westward. Owing to the gyroradius loss of entered solar wind ions, a plasma belt with the dawn-dusk asymmetry thus forms gradually in the inner magnetosphere, generating an outward gradient of plasma pressure within a downstream radial distance of 1.2–1.4 R_M. The presence of this outward plasma pressure drives an eastward current encircling the planet on the night side and closing the Chapman–Ferraro current on the dayside.

5 Conclusion.

Both data analysis and simulations in our study consistently demonstrate that there is no significant Earth-like ring current drifting westward around Mercury but reveal that there is an encircling eastward current on the night side. The discovery of the EC extends our knowledge of Mercury's magnetospheric current system (Figure 3c) and shows that Mercury's small magnetosphere should not be treated simply as a scaled-down version of Earth's magnetosphere. On the contrary, it may well be a unique natural laboratory for space plasma exploration. Our discovery of EC also offers a new source of the external field which could be important in regulating the interior dynamo processes, because it was theoretically anticipated that the field by external magnetospheric current could affect the dynamo (Glassmeier et al., 2007 and Heyner et al., 2011). In addition, our study may have important implications for studying the magnetospheres of exoplanets. One good example is the TRAPPIST-1 system (Dong et al., 2017, 2018), with its seven Earth-sized exoplanets, in which, those close-in exoplanets are expected to be tidally locked to their star and thus may have weak intrinsic magnetic fields like Mercury. The

upcoming data from the BepiColombo mission, with its dual spacecraft carrying state-of-art instruments, could help uncover the formation and evolution of EC more deeply (Benkhoff et al., 2021; Milillo et al., 2021).

Acknowledgments

We are grateful to the teams of the MESSENGER Magnetometer (MAG) and the Fast Imaging Plasma Spectrometer (FIPS) for providing the scientific data from those instruments used in this study.

Funding: This work was supported by the the Strategic Priority Research Program of Chinese Academy of Sciences (Grant No. XDB 41000000), the National Natural Science Foundation of China (Grant Nos. 41922031, 41774188), the Key Research Program of the Institute of Geology & Geophysics, CAS (Grant Nos. IGGCAS-201904, IGGCAS-202102), and the Key Research Program of Chinese Academy of Sciences (Grant No. ZDBS-SSW-TLC00103). S. Fatemi acknowledges support from the Swedish Research Council (VR) grant 2018-03454 and the Swedish National Space Agency (SNSA) grant 115/18. The computations are enabled by resources provided by the Swedish National Infrastructure for Computing (SNIC) at the High Performance Computing Center North (HPC2N), Umeå University, Sweden, and NVIDIA's Academic Hardware Grant Program.

Author contributions: Z.J.R. offered the physical idea and contributed to the draft of manuscript. Z.S. performed the data analysis, contributed to data graphics, and prepared the draft of manuscript. S.F., C.F.D. and L.W. contributed to the simulations of how Mercury interacts with the solar wind. K.L. contributed to polishing language. J.A.S. and J.Z. contributed to data

interpretation and revision of manuscript. J.M.R. contributed to guaranteeing data quality. M.H., C.J.Y., S.B. and Y.W. contributed to the revision of manuscript.

Competing interests: Authors declare that they have no competing interests.

Data availability: The Magnetometer data is available at https://pds-ppi.igpp.ucla.edu/search/view/?f=yes&id=pds://PPI/MESS-E_V_H_SW-MAG-3-CDR-CALIBRATED-V1.0/DATA/MSO. The NTP (proton number density, temperature, and thermal pressure) dataset from the FIPS is available at https://pds-ppi.igpp.ucla.edu/search/view/?f=yes&id=pds://PPI/mess-epps-fips-derived/data/ntp.

References

1. Aizawa, S., Griton, L. S., Fatemi, S., Exner, W., Deca, J., Pantellini, F., ... & Usui, H. (2021). Cross-comparison of global simulation models applied to Mercury's dayside magnetosphere. Planetary and Space Science, 198, 105176.
2. Alfvén, H. & Fälthammar, C.G. (1963). *Cosmical Electrodynamics.* Oxford Press.
3. Anderson, B. J., Acuña, M. H., Lohr, D. A., Scheifele, J., Raval, A., Korth, H., & Slavin, J. A. (2007). The Magnetometer instrument on MESSENGER. In The MESSENGER mission to Mercury (pp. 417-450). Springer, New York, NY.
4. Anderson, B. J., Johnson, C. L., Korth, H., Purucker, M. E., Winslow, R. M., Slavin, J. A., ... & Zurbuchen, T. H. (2011). The global magnetic field of Mercury from MESSENGER orbital observations. Science, 333(6051), 1859-1862.
5. Anderson, B. J., Slavin, J. A., Korth, H., Boardsen, S. A., Zurbuchen, T. H., Raines, J. M., ... & Solomon, S. C. (2011). The dayside magnetospheric boundary layer at Mercury. Planetary and Space Science, 59(15), 2037-2050.
6. Andrews, G. B., Zurbuchen, T. H., Mauk, B. H., Malcom, H., Fisk, L. A., Gloeckler, G., ... & Raines, J. M. (2007). The Energetic Particle and Plasma Spectrometer instrument on the MESSENGER spacecraft. Space Science Reviews, 131(1), 523-556.
7. Benkhoff, J., Murakami, G., Baumjohann, W., Besse, S., Bunce, E., Casale, M., ... & Zender, J. (2021). BepiColombo-Mission Overview and Science Goals. Space Science Reviews, 217(8), 1-56.

8. Daglis, I. A. (2006). Ring current dynamics. Space science reviews, 124(1), 183-202.
9. Dong, C., Lingam, M., Ma, Y., & Cohen, O. (2017). Is Proxima Centauri b habitable? A study of atmospheric loss. The Astrophysical Journal Letters, 837(2), L26.
10. Dong, C., Jin, M., Lingam, M., Airapetian, V. S., Ma, Y., & van der Holst, B. (2018). Atmospheric escape from the TRAPPIST-1 planets and implications for habitability. Proceedings of the National Academy of Sciences, 115(2), 260-265.
11. Dong, C., Wang, L., Hakim, A., Bhattacharjee, A., Slavin, J. A., DiBraccio, G. A., & Germaschewski, K. (2019). Global ten- moment multifluid simulations of the solar wind interaction with mercury: From the planetary conducting core to the dynamic magnetosphere. Geophysical Research Letters, 46(21), 11584-11596.
12. Fatemi, S., Poppe, A. R., Delory, G. T., & Farrell, W. M. (2017, May). AMITIS: A 3D GPU-based hybrid-PIC model for space and plasma physics. In Journal of Physics: Conference Series (Vol. 837, No. 1, p. 012017). IOP Publishing.
13. Fatemi, S., Poirier, N., Holmström, M., Lindkvist, J., Wieser, M., & Barabash, S. (2018). A modelling approach to infer the solar wind dynamic pressure from magnetic field observations inside Mercury's magnetosphere. Astronomy & Astrophysics, 614, A132.
14. Fatemi, S., & Poppe, A. R. (2018). Solar wind plasma interaction with asteroid 16 Psyche: Implication for formation theories. Geophysical Research Letters, 45(1), 39-48.
15. Fatemi, S., Poppe, A. R., & Barabash, S. (2020). Hybrid simulations of solar wind proton precipitation to the surface of Mercury. Journal of Geophysical Research: Space Physics, 125(4), e2019JA027706.
16. Fujimoto, M., Terasawa, T., & Mukai, T. (1997). The cold-dense plasma sheet: A GEOTAIL perspective. Space Science Reviews, 80(1), 325-339.
17. Fuqua Haviland, H., Poppe, A. R., Fatemi, S., Delory, G. T., & De Pater, I. (2019). Time-dependent hybrid plasma simulations of lunar electromagnetic induction in the solar wind. Geophysical Research Letters, 46(8), 4151-4160.
18. Gershman, D. J., Slavin, J. A., Raines, J. M., Zurbuchen, T. H., Anderson, B. J., Korth, H., ... & Solomon, S. C. (2013). Magnetic flux pileup and plasma depletion in Mercury's subsolar magnetosheath. Journal of Geophysical Research: Space Physics, 118(11), 7181-7199.
19. Glassmeier, K. H. (2000). Currents in Mercury's magnetosphere. GEOPHYSICAL MONOGRAPH-AMERICAN GEOPHYSICAL UNION, 118, 371-380.
20. Glassmeier, K. H., Auster, H. U., & Motschmann, U. (2007). A feedback dynamo generating Mercury's magnetic field. Geophysical research letters, 34(22).
21. Hasegawa, H., Fujimoto, M., Phan, T. D., Reme, H., Balogh, A., Dunlop, M. W., ... & TanDokoro, R. (2004). Transport of solar wind into Earth's magnetosphere through rolled-up Kelvin–Helmholtz vortices. Nature, 430(7001), 755-758.
22. Herčík, D., Trávníček, P.M., Štverák, Š. & Hellinger, P. (2016). Properties of Hermean plasma belt: Numerical simulations and comparison with MESSENGER data. Journal of Geophysical Research: Space Physics, 121(1), 413-431.

23. Heyner, D., Wicht, J., Gómez-Pérez, N., Schmitt, D., Auster, H. U., & Glassmeier, K. H. (2011). Evidence from numerical experiments for a feedback dynamo generating Mercury's magnetic field. Science, 334(6063), 1690-1693.

24. Ho, G. C., Starr, R. D., Krimigis, S. M., Vandegriff, J. D., Baker, D. N., Gold, R. E., ... & Solomon, S. C. (2016). MESSENGER observations of suprathermal electrons in Mercury's magnetosphere. Geophysical Research Letters, 43(2), 550-555.

25. Kallio, E., Wurz, P., Killen, R., McKenna-Lawlor, S., Milillo, A., Mura, … & Ip, W.H. (2008). On the impact of multiply charged heavy solar wind ions on the surface of Mercury, the Moon and Ceres. Planetary and Space Science, 56(11), 1506-1516.

26. Korth, H., Anderson, B. J., Johnson, C. L., Winslow, R. M., Slavin, J. A., Purucker, M. E., ... & McNutt Jr, R. L. (2012). Characteristics of the plasma distribution in Mercury's equatorial magnetosphere derived from MESSENGER Magnetometer observations. Journal of Geophysical Research: Space Physics, 117(A12).

27. Korth, H., Anderson, B. J., Gershman, D. J., Raines, J. M., Slavin, J. A., Zurbuchen, T. H., ... & McNutt Jr, R. L. (2014). Plasma distribution in Mercury's magnetosphere derived from MESSENGER Magnetometer and Fast Imaging Plasma Spectrometer observations. Journal of Geophysical Research: Space Physics, 119(4), 2917-2932.

28. Le, G., Russell, C. T., & Takahashi, K. (2004, April). Morphology of the ring current derived from magnetic field observations. In Annales Geophysicae (Vol. 22, No. 4, pp. 1267-1295). Copernicus GmbH.

29. Liemohn, M. W., Ganushkina, N. Y., Katus, R. M., De Zeeuw, D. L., & Welling, D. T. (2013). The magnetospheric banana current. Journal of Geophysical Research: Space Physics, 118(3), 1009-1021.

30. Milillo, A., Fujimoto, M., Murakami, G., Benkhoff, J., Zender, J., Aizawa, S., ... & Wahlund, J. E. (2020). Investigating Mercury's environment with the two-spacecraft BepiColombo mission. Space science reviews, 216(5), 1-78.

31. Mura, A., Orsini, S., Milillo, A., Delcourt, D., Massetti, S. & De Angelis, E. (2005). Dayside H+ circulation at Mercury and neutral particle emission. Icarus, 175(2), 305-319.

32. Müller, J., Simon, S., Wang, Y. C., Motschmann, U., Heyner, D., Schüle, J., ... & Pringle, G. J. (2012). Origin of Mercury's double magnetopause: 3D hybrid simulation study with AIKEF. Icarus, 218(1), 666-687.

33. Ness, N. F., Behannon, K. W., Lepping, R. P., Whang, Y. C., & Schatten, K. H. (1974). Magnetic field observations near Mercury: Preliminary results from Mariner 10. Science, 185(4146), 151-160.

34. Northrop, T. G. (1963). Adiabatic charged- particle motion. Reviews of Geophysics, 1(3), 283-304.

35. Paral, J., & Rankin, R. (2013). Dawn–dusk asymmetry in the Kelvin–Helmholtz instability at Mercury. Nature Communications, 4(1), 1-5.

36. Parker, E. N. (1957). Newtonian development of the dynamical properties of ionized gases of low density. Physical Review, 107(4), 924.

37. Parks, G.K. (2004) *Physics of space plasmas: an introduction.* Westview Press.

38. Raines, J. M., Slavin, J. A., Zurbuchen, T. H., Gloeckler, G., Anderson, B. J., Baker, D. N., ... & McNutt Jr, R. L. (2011). MESSENGER observations of the plasma environment near Mercury. Planetary and Space Science, 59(15), 2004-2015.

39. Raines, J. M., Gershman, D. J., Zurbuchen, T. H., Sarantos, M., Slavin, J. A., Gilbert, J. A., ... & Solomon, S. C. (2013). Distribution and compositional variations of plasma ions in Mercury's space environment: The first three Mercury years of MESSENGER observations. Journal of Geophysical Research: Space Physics, 118(4), 1604-1619.

40. Rasca, A. P., Fatemi, S., Farrell, W. M., Poppe, A. R., & Zheng, Y. (2021). A double disturbed lunar plasma wake. Journal of Geophysical Research: Space Physics, 126(2), e2020JA028789.

41. Rong, Z. J., Ding, Y., Slavin, J. A., Zhong, J., Poh, G., Sun, W. J., ... & Shen, C. (2018). The magnetic field structure of Mercury's magnetotail. Journal of Geophysical Research: Space Physics, 123(1), 548-566.

42. Schriver, D., Trávníček, P. M., Anderson, B. J., Ashour- Abdalla, M., Baker, D. N., Benna, M., ... & Zurbuchen, T. H. (2011). Quasi- trapped ion and electron populations at Mercury. Geophysical research letters, 38(23).

43. Shen, C., Yang, Y. Y., Rong, Z. J., Li, X., Dunlop, M., Carr, C. M., ... & Zeng, G. (2014). Direct calculation of the ring current distribution and magnetic structure seen by Cluster during geomagnetic storms. Journal of Geophysical Research: Space Physics, 119(4), 2458-2465.

44. Slavin, J. A., Acuña, M. H., Anderson, B. J., Baker, D. N., Benna, M., Gloeckler, G., ... & Zurbuchen, T. H. (2008). Mercury's magnetosphere after MESSENGER's first flyby. science, 321(5885), 85-89.

45. Solomon, S. C., McNutt, R. L., Gold, R. E., & Domingue, D. L. (2007). MESSENGER mission overview. Space Science Reviews, 131(1), 3-39.

46. Song, P., & Russell, C. T. (1992). Model of the formation of the low- latitude boundary layer for strongly northward interplanetary magnetic field. Journal of Geophysical Research: Space Physics, 97(A2), 1411-1420.

47. Sun, W. J., Fu, S. Y., Slavin, J. A., Raines, J. M., Zong, Q. G., Poh, G. K., & Zurbuchen, T. H. (2016). Spatial distribution of Mercury's flux ropes and reconnection fronts: MESSENGER observations. Journal of Geophysical Research: Space Physics, 121(8), 7590-7607.

48. Sundberg, T., Boardsen, S. A., Slavin, J. A., Anderson, B. J., Korth, H., Zurbuchen, T. H., ... & Solomon, S. C. (2012). MESSENGER orbital observations of large- amplitude Kelvin-Helmholtz waves at Mercury's magnetopause. Journal of Geophysical Research: Space Physics, 117(A4).

49. Terasawa, T., Fujimoto, M., Mukai, T., Shinohara, I., Saito, Y., Yamamoto, T., ... & Lepping, R. P. (1997). Solar wind control of density and temperature in the near- Earth plasma sheet: WIND/GEOTAIL collaboration. Geophysical research letters, 24(8), 935-938.

50. Walsh, B. M., Ryou, A. S., Sibeck, D. G., & Alexeev, I. I. (2013). Energetic particle dynamics in Mercury's magnetosphere. Journal of Geophysical Research: Space Physics, 118(5), 1992-1999.

51. Winslow, R. M., Anderson, B. J., Johnson, C. L., Slavin, J. A., Korth, H., Purucker, M. E., ... & Solomon, S. C. (2013). Mercury's magnetopause and bow shock from MESSENGER Magnetometer observations. Journal of Geophysical Research: Space Physics, 118(5), 2213-2227.

52. Yagi, M., Seki, K., Matsumoto, Y., Delcourt, D. C., & Leblanc, F. (2010). Formation of a sodium ring in Mercury's magnetosphere. Journal of Geophysical Research: Space Physics, 115(A10).

53. Yang, Y. Y., Shen, C., Dunlop, M., Rong, Z. J., Li, X., Angelopoulos, V., ... & Ji, Y. (2016). Storm time current distribution in the inner equatorial magnetosphere: THEMIS observations. Journal of Geophysical Research: Space Physics, 121(6), 5250-5259.

54. Zhong, J., Wan, W. X., Slavin, J. A., Wei, Y., Lin, R. L., Chai, L. H., ... & Han, X. H. (2015). Mercury's three- dimensional asymmetric magnetopause. Journal of Geophysical Research: Space Physics, 120(9), 7658-7671.

55. Zurbuchen, T. H., Raines, J. M., Slavin, J. A., Gershman, D. J., Gilbert, J. A., Gloeckler, G., ... & Solomon, S. C. (2011). MESSENGER observations of the spatial distribution of planetary ions near Mercury. Science, 333(6051), 1862-1865.

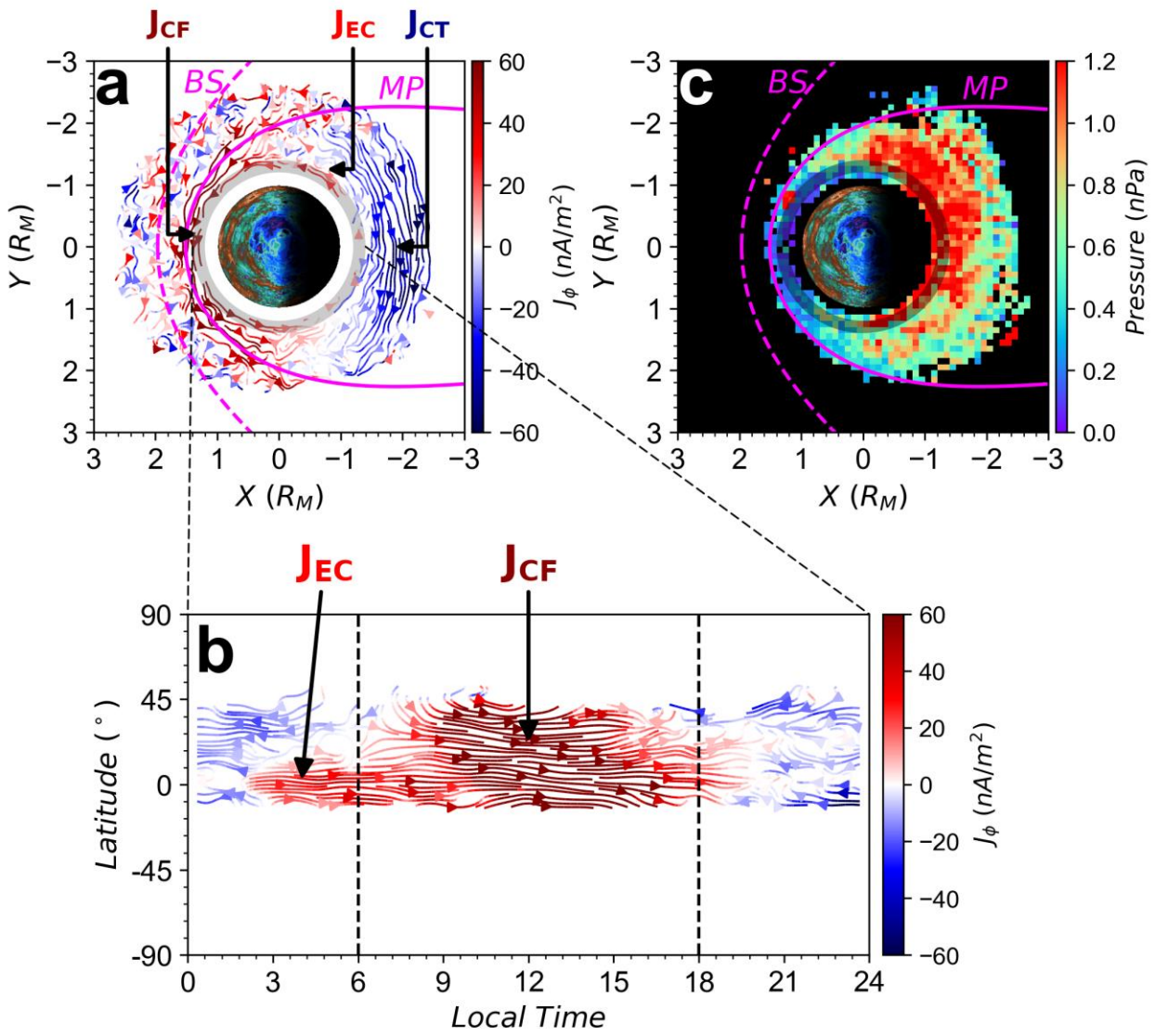

Figure 1. The average distribution of current density computed by $\nabla \times \boldsymbol{B}$ from MESSENGER data and pressure distribution from FIPS NTP data set**. a.** The distribution of current density in the magnetic equatorial plane ($|z|$<0.05 R_M)**.** The nominal shapes of bow shock (BS, Winslow et al, 2013) and magnetopause (MP, Zhong et al., 2015) are denoted as dashed and solid magenta lines, respectively. The streamlines with arrows, denoting the flows of current density, are colored by the azimuth component of current density, $\boldsymbol{J}_\phi$. The positive (negative) $\boldsymbol{J}_\phi$, colored by red (blue), indicates the eastward (westward) current densities. $\boldsymbol{J}_{CF}$ labels the Chapman–Ferraro current at the dayside magnetopause, $\boldsymbol{J}_{CT}$ labels the magnetotail cross-tail current, and $\boldsymbol{J}_{EC}$ labels the eastward current that we found in the nightside magnetosphere. The torus with radial distances of 1.2–1.4 R_M is shaded. **b.** The average distribution of current density on the surface of a concentric spherical shell whose cross-section by the magnetic equatorial plane is shaded as the torus in **a**. The format of streamlines is the same as that in **a**. The dayside is indicated by the local time (LT) range 06:00–18:00 between the two vertical dashed lines. **c.** The distribution of plasma pressure derived from FIPS NTP data set (see subsection 2.2). The corresponding notations are the same as those in **a**.

Table 1. The input parameters of the upstream solar wind for simulations. IMF B_x, IMF B_y, and IMF B_z are the three components of the IMF along the x-axis, y-axis, and z-axis respectively; P_{dyn} is the dynamic pressure of the upstream solar wind; V_x is the flow speed of the solar wind along the x-axis; N_0 is the number density of protons in the solar wind; β is the plasma Beta which is the ratio of plasma pressure to magnetic pressure; V_{cs} is the speed of sound in the solar wind.

	IMF B_x (nT)	IMF B_y (nT)	IMF B_z (nT)	P_{dyn} (nPa)	V_x (km/s)	N_0 (#/cm^3)	β	V_{cs} (km/s)
Case 1	+17.55	0	4	6.82	-370	30	0.9	62.29
Case 2	+17.55	0	-4	6.82	-370	30	0.9	62.29
Case 3	+17.55	0	4	17.93	-600	30	0.9	62.29

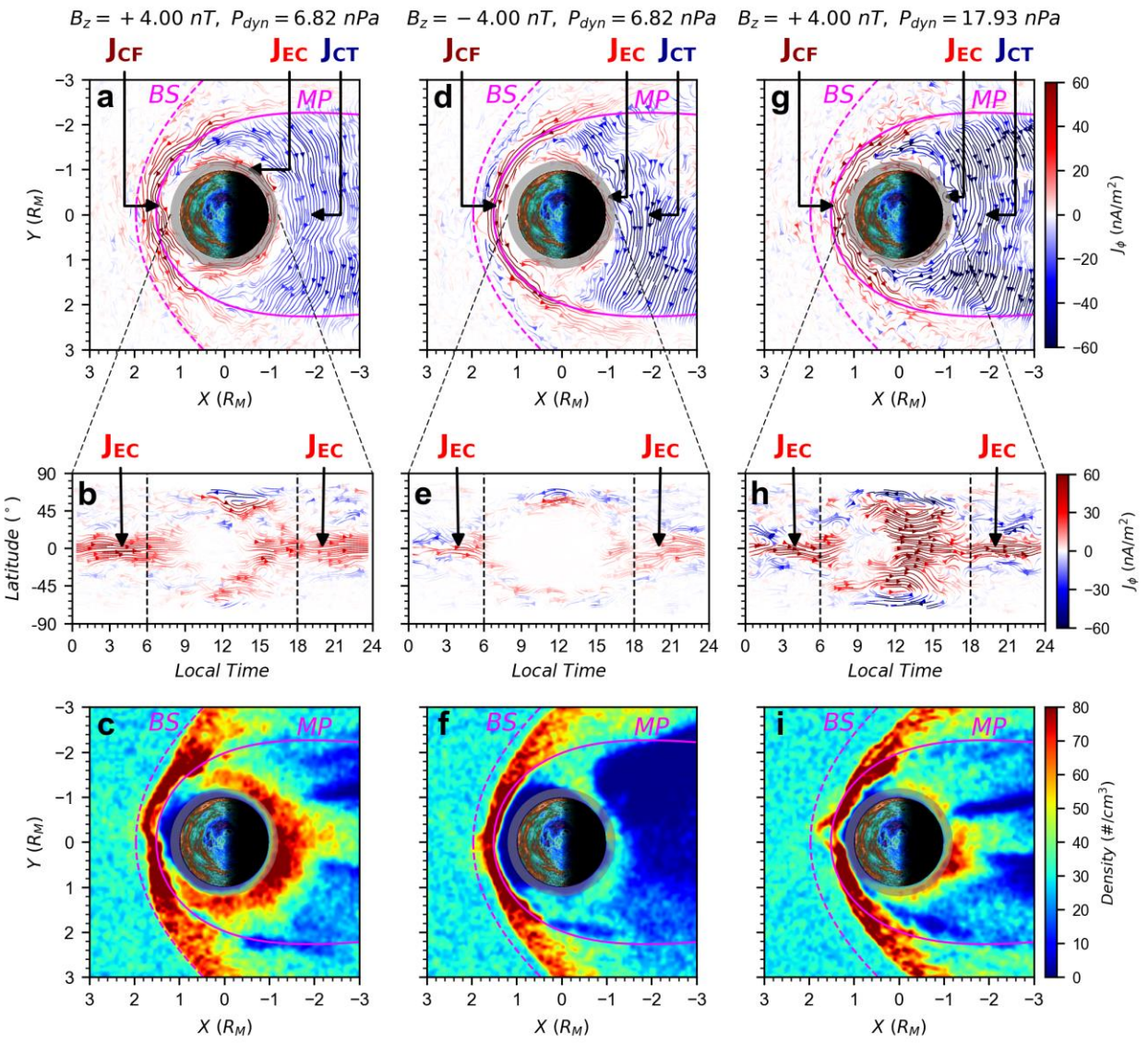

Figure 2. The simulated current density and proton number density for the three cases listed in Table 1 for northward IMF(**a-c**), southward IMF(**d-f**), and the higher dynamic pressure of solar wind (**g-i**). The upper panels show the distributions of current density in the cut of the magnetic equatorial plane (**a**, **d**, **g**); the middle panels show the streamlines of current density on a spherical surface which covers the radial distances of 1.0–1.2 R_M (**b**, **e**, **h**); the lower panels show the corresponding distributions of proton number density (**c**, **f**, **i**). The torus with radial distances of 1.0–1.2 R_M is shaded.

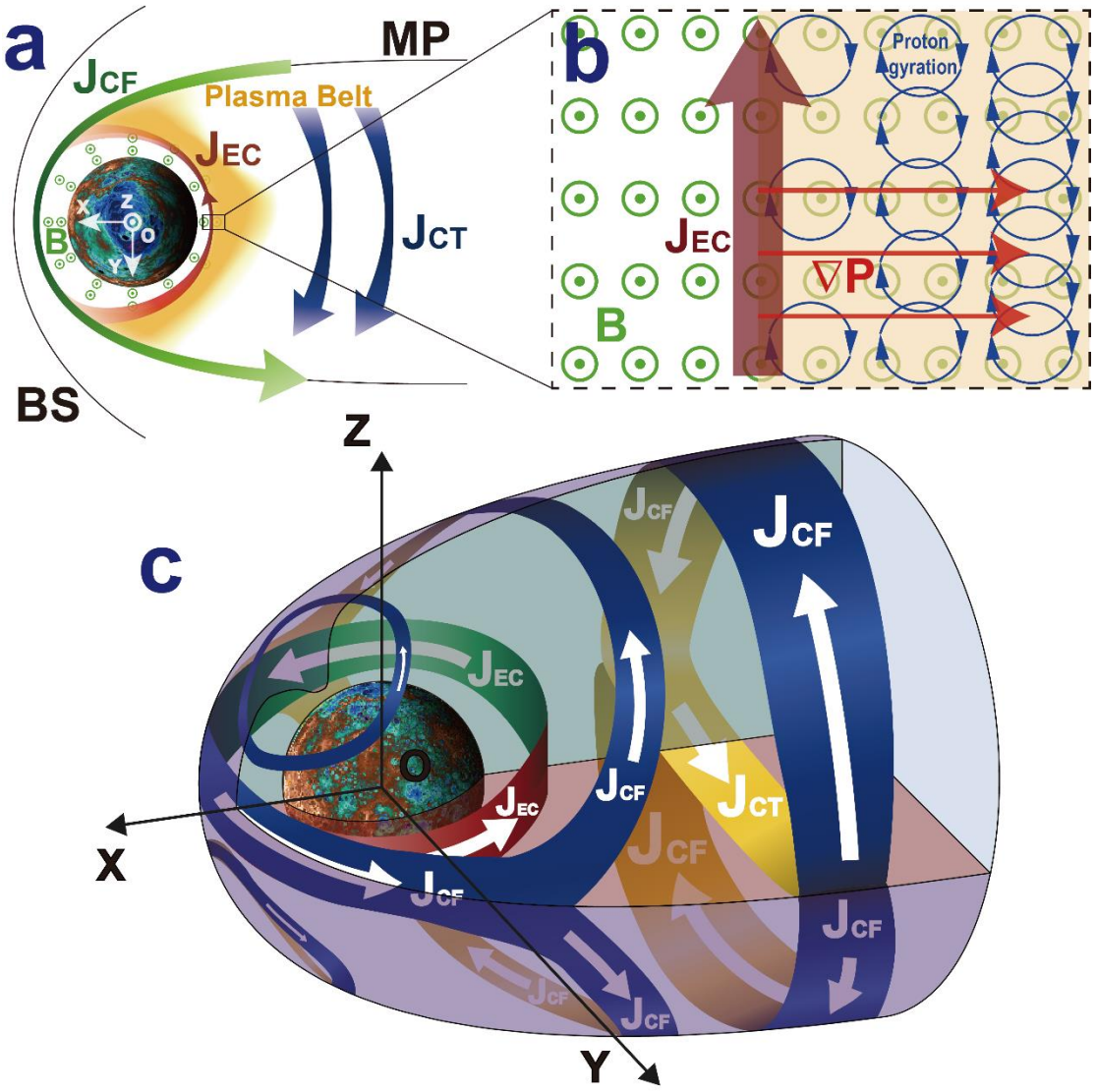

Figure 3. The mechanism of eastward current and the magnetospheric current system of Mercury. **a**. Diagram to illustrate the formation of the EC in the magnetic equatorial plane. The night side plasma pressure is yellow-shaded. The direction of the magnetic field (***B***, green-circled dots) points northward. The dayside Chapman–Ferraro current ($\boldsymbol{J}_{CF}$), magnetotail cross-tail current ($\boldsymbol{J}_{CT}$), and night side eastward current ($\boldsymbol{J}_{EC}$) are denoted as green, blue, and brick-red lines with arrows, respectively. **b**. The zoomed-in diagram shows the generation of the EC at midnight. The directions of the plasma pressure gradient (∇P) near Mercury are outward, denoted as red arrows. The gyrations of protons are denoted by blue circles with arrows. **c**. Diagram of the magnetospheric current system of Mercury. The current pattern consists of the magnetopause current or Chapman–Ferraro current ($\boldsymbol{J}_{CF}$), the cross-tail current ($\boldsymbol{J}_{CT}$) in the magnetotail current sheet, and the eastward current ($\boldsymbol{J}_{EC}$) that we have found.